Thermal Stimulus Task fMRI in the Cervical Spinal Cord at 7 Tesla

Alan C. Seifert[1,2,3,*], Junqian Xu[4], Yazhuo Kong[5,6], Falk C. Eippert[5,7], Karla L. Miller[5], Irene Tracey[5], S. Johanna Vannesjo[5,8]

[1]Biomedical Engineering and Imaging Institute, Icahn School of Medicine at Mount Sinai, New York, NY USA

[2]Department of Diagnostic, Molecular, and Interventional Radiology, Icahn School of Medicine at Mount Sinai, New York, NY USA

[3]Graduate School of Biomedical Sciences, Icahn School of Medicine at Mount Sinai, New York, NY USA

[4]Departments of Radiology and Psychiatry, Baylor College of Medicine, Houston, TX USA

[5]Wellcome Centre for Integrative Neuroimaging, FMRIB, Nuffield Department of Clinical Neurosciences, University of Oxford, Oxford, UK

[6]Institute of Psychology, Chinese Academy of Sciences, Beijing, China

[7]Max Planck Institute for Human Cognitive and Brain Sciences, Leipzig, Germany

[8]Department of Physics, Norwegian University of Science and Technology (NTNU), Trondheim, Norway

*Corresponding author:
Alan C. Seifert:
E-mail: alan.seifert@mssm.edu
Address: One Gustave L. Levy Place
Box 1234
New York, NY 10029
Phone: 212-824-8456
Fax: 646-537-9589

Running Title: 7T CSC Thermal Task fMRI

Submitted to:

Submission Type: Research Article (Full Paper)

Disclosures: All authors state that they have no conflicts of interest.

Preliminary results from this manuscript have previously been presented in the following conference abstracts:

Seifert AC, Vannesjo SJ. Spatial Specificity of BOLD Signal in the Spinal Cord at 7T Using a Noxious Thermal Stimulus. Proceedings of the International Society for Magnetic Resonance in Medicine 2020:1168.

Seifert AC, Vannesjo SJ. Comparison of Physiological Noise Models for Thermal Stimulus fMRI in the Cervical Spinal Cord at 7T. Proceedings of the International Society for Magnetic Resonance in Medicine 2022:1462.

Abstract

Purpose: Although functional MRI is widely applied in the brain, fMRI of the spinal cord is more technically demanding. Proximity to the vertebral column and lungs results in strong spatial inhomogeneity and temporal fluctuations in B_0. Increasing field strength enables higher spatial resolution and improved sensitivity to BOLD signal, but amplifies the effects of B_0 inhomogeneity. In this work, we present the first stimulus task fMRI in the spinal cord at 7 T. Further, we compare the performance of single-shot and multi-shot 2D EPI protocols, as they differ in sensitivity to spatial and temporal B_0 inhomogeneity.

Methods: The cervical spinal cords of 11 healthy volunteers were scanned at 7 T using single-shot 2D EPI at 0.75 mm in-plane resolution and multi-shot 2D EPI at 0.75 and 0.6 mm in-plane resolutions. For each protocol, the BOLD response to thirteen 10-second noxious thermal stimuli applied to the right thumb was acquired in a 10-minute fMRI run. Image quality, temporal SNR, and BOLD activation (percent signal change and z-stat) at both individual- and group-level were evaluated between the protocols.

Results: Temporal SNR was highest in single-shot and multi-shot 0.75 mm protocols. In group-level analyses, activation clusters appeared in all protocols in the ipsilateral dorsal quadrant at the expected C6 neurological level. In individual-level analyses, activation clusters at the expected level were detected in some, but not all subjects and protocols. Single-shot 0.75 mm generally produced the highest mean z-statistic, while multi-shot 0.60 mm produced the best-localized activation clusters and the least geometric distortion. Larger than expected within-subject segmental variation of BOLD activation along the cord was observed.

Conclusion: Group-level sensory task fMRI of the cervical spinal cord is feasible at 7 T with single-shot or multi-shot EPI. The best choice of protocol will likely depend on the relative importance of sensitivity to activation versus spatial localization of activation for a given experiment.

Highlights

- First stimulus task fMRI results in the spinal cord at 7 T
- Single-shot 0.75 mm 2D EPI produced the highest mean z-statistic
- Multi-shot 0.60 mm 2D EPI provided the best-localized activation and least distortion
- Group-level sensory task fMRI of the spinal cord is feasible at 7 T

Key Words

Spinal cord fMRI, 7T MRI, ultra-high field, fMRI

Introduction

The spinal cord houses many scientifically and clinically important neural circuits, such as central pattern generators related to locomotion (1), sensorimotor reflex arcs, and circuits involved in the modulation of nociception (2). Although functional MRI is a well-established and widely-applied imaging modality to probe neural activity in the brain, fMRI of the spinal cord is more technically demanding.

The adult human spinal cord is approximately 15 mm in diameter at its widest point, with gray matter structures only approximately 1-4 mm wide. High spatial resolution is therefore required to image the blood oxygenation level-dependent (BOLD) signal in the spinal cord. In addition to its small size, several additional factors complicate fMRI of the spinal cord. The spinal cord is directly adjacent to the vertebral column, which is composed of alternating vertebral bones and soft tissues that differ in magnetic susceptibility. The spatially periodic B_0 inhomogeneities created in the spinal cord by the vertebral column cannot be adequately cancelled by a counter-field generated by shim currents from the scanner's spherical harmonic-based shim coils, leaving residual focal B_0 inhomogeneities near the intervertebral junctions. The spinal cord is also near the lungs, whose volume and concentration of paramagnetic O_2 varies over time due to respiration. This creates temporal fluctuations in B_0 in the spinal cord (3), producing frequency variation that can exceed 100 Hz at C7 (4). These spatially and temporally varying B_0 inhomogeneities produce geometric distortion and signal loss, as well as apparent motion between volumes in the time series. Pulsatile rostral-caudal flow of cerebrospinal fluid (CSF) over the cardiac cycle, and intermittent swallowing and motion, can also contribute nuisance variation to fMRI signal (5,6).

Increasing the static magnetic field (B_0) improves signal to noise ratio (SNR), which translates to higher achievable spatial resolution. Increased B_0 also increases sensitivity to BOLD signal in gradient-echo (GRE) EPI, leading to better sensitivity and spatial specificity (7,8). These advantages motivate the use of 7 T fMRI to investigate circuits in the spinal cord. However, several difficulties are magnified at or unique to 7 T. As field strength increases, susceptibility-mediated effects are magnified. Hence, although SNR and BOLD signal are enhanced, the geometric distortions and signal loss associated with B_0 inhomogeneity arising from the lungs and vertebral column are also intensified (9,10). 7 T scanners also lack a body RF transmit coil, and standard head RF coils do not cover the cervical spinal cord, which necessitates specialized RF hardware for the spinal cord that remains only accessible at a handful of research centers (11).

These challenges have hampered the development of spinal cord fMRI at 7 T, despite the potential advantages of higher field strength. To date there are only three studies of spinal cord fMRI at 7 T (12–14) all of which are resting-state fMRI studies, investigating connectivity between gray matter regions in the absence of external stimuli or motor tasks. A significant motivation for the development of spinal cord fMRI methods, however, is to study pain processing in healthy and pathological states (15–20). This involves measuring the BOLD response to external painful stimuli. There is thus a need for investigating the potential of 7 T for task-based spinal cord fMRI.

One important step towards fully realizing the potential benefits of 7 T is to establish suitable acquisition sequences and protocols that yield high BOLD sensitivity while being sufficiently robust against the challenges posed by static and dynamic B_0 inhomogeneities. At lower field strengths, various sequences have been investigated for spinal cord fMRI. Single-shot echo-planar imaging (EPI) is currently the dominant method for fMRI in the human spinal cord, as in the brain. The initial motor task fMRI studies in the cervical spinal cord, however, used a variety of pulse sequences, including fast low-angle shot (FLASH) sequences at 1.5 T (21) and 3 T (22), multi-shot gradient echo (GRE) EPI at 1.5 T (23), spin-echo EPI at 1.5 T (24), and single-shot fast spin echo at 1.5 T (25,26). Spin-echo-based pulse sequences continued to be used for fMRI in the spinal cord at 1.5 T based on signal enhancement by extravascular water protons (SEEP) contrast for many years (27,28). Work on BOLD fMRI in the spinal cord by multiple groups over the next several years focused mainly on 2D single-shot (29–35) and 3D multi-shot (36) GRE EPI at 1.5 T and 3 T.

Single-shot EPI sequences are heavily affected by geometric distortion and signal loss caused by static B_0 inhomogeneity. Multi-shot EPI sequences have strong potential to reduce these artifacts by shortening the echo train length and echo time. In the previous 7 T resting-state studies, highly segmented multi-shot 3D EPI with very short echo train lengths was used (12,13,37), yielding images largely uncorrupted by signal loss and distortion near intervertebral junctions. However, the transition from single-shot to multi-shot EPI entails a penalty in volume acquisition time (VAT), which can reduce sensitivity to BOLD activation by reducing the number of observation time points for a given scan duration. Multi-shot EPI is also more sensitive to dynamic B_0 field fluctuations, resulting in variable ghosting between volumes in the time series, which can reduce the temporal SNR (38). In single-shot EPI, on the other hand, time-variable B_0 fields (at the respiratory time-scale) largely translate into apparent motion in the images, which can be addressed by retrospective motion correction. Considering the relative advantages and disadvantages of single-shot vs. multi-shot EPI sequences, it is not apparent which is more

suitable for fMRI of the spinal cord at ultra-high field.

In this work, we present the first stimulus task fMRI in the cervical spinal cord at 7 T and compare the performance of one single-shot 2D EPI and two multi-shot 2D EPI protocols in terms of sensitivity and specificity to stimulus-related activation.

Methods

The cervical spinal cords (C4-C7 vertebral levels, approximately corresponding to spinal cord segments C5-C8) of eleven healthy volunteers (ages 22-39, 5 males, 6 females) were scanned using a 7 T whole-body MRI system (Magnetom 7 T AS, Siemens Healthineers, Erlangen, Germany) equipped with a G_{max} = 70 mT/m and maximum slew rate = 200 mT/m/ms gradient coil and a single-channel four-element transmit, 22-channel receive array brainstem and cervical spine radiofrequency (RF) coil (39). All imaging experiments were performed under an IRB-approved protocol and in full compliance with all applicable human subject protection regulations. Shim adjustment (up to 2nd order) was performed during free breathing. B_1^+ adjustment was performed by setting transmit reference voltage to 250 V, a level which avoids clipping of RF pulses, and produces correctly-calibrated RF pulses in most subjects at approximately the level of the C5/6 intervertebral disc. Anatomical T_1-weighted sagittal MP2RAGE (40) images at 0.7 mm isotropic resolution were acquired for every subject to aid in registration to template space.

One single-shot 2D EPI protocol at 0.75 mm in-plane resolution and two multi-shot 2D EPI protocols at 0.75 mm and 0.6 mm in-plane resolution were used (Figure 1). These three protocols will be abbreviated SS75, MS75, and MS60, respectively. Each protocol was optimized independently, rather than attempting to match parameters between protocols. Research pulse sequences were used for both the single-shot and multi-shot acquisitions. (At the time of this study, a multi-shot 3D EPI pulse sequence analogous to what was used in references (12–14) was not available on our scanner platform.) In all protocols, the FOV was intentionally centered towards the back of the neck to include posterior neck muscles, which, due to their greater distance from the trachea and esophagus, serve as spatial landmarks that are relatively robust to swallowing to aid subsequent motion correction.

In the single-shot EPI, a single saturation slab was placed anterior to the spinal cord for outer volume suppression, thereby reducing the required echo-train length. For in-plane acceleration using generalized autocalibrating partially parallel acquisition (GRAPPA) (41), 52 lines of autocalibration signal reference data were acquired using GRE (42), which has been shown to be

168 optimal for single-shot EPI in the spinal cord at 7 T (43). Partial Fourier (factor 6/8) acquisition
169 was judged to be necessary in single-shot EPI to further reduce TE to avoid excessive signal loss
170 due to through-slice dephasing. Image reconstruction of the single-shot EPI was performed
171 online with the standard reconstruction pipeline of the manufacturer, including Nyquist ghost
172 correction based on a three-line navigator.

173 The multi-shot protocols were acquired without a spatial saturation slab due to SAR limitations
174 given the shorter per-shot TR. Extending the volume acquisition time to accommodate spatial
175 saturation was judged to be an unfavorable tradeoff. Therefore, a larger FOV had to be acquired
176 in the multi-shot protocols, than in the single-shot protocol, to encompass signal from the entire
177 neck. Note that phase-encode FOVs cannot be defined to be larger than readout-encode FOV,
178 and the readout-encode FOV can be enlarged with no SNR or timing penalties. For this reason,
179 the FOV in the multi-shot protocol was set larger in the readout (right-left) dimension than in the
180 single-shot protocol to achieve the intended increase in the phase-encode FOV. Phase-encoding
181 in the left-right dimension is undesirable because the patterns of spatial distortion in the spinal
182 cord would be asymmetric across the left-right dimension of the spinal cord. Unlike the single-
183 shot sequence, the custom multi-shot sequence did not allow for GRAPPA acceleration via the
184 console, therefore the FOV in the phase-encode dimension was set to half of the readout FOV in
185 the multi-shot protocols to achieve the intended phase-encode undersampling (Fig. 1). Image
186 reconstruction of the multi-shot acquisitions was performed offline, with an iterative conjugate
187 gradient SENSE algorithm (44). The coil sensitivities were estimated based on a low-resolution
188 gradient-echo acquisition. For SNR-optimal coil combination, the noise correlation between coils
189 was calculated based on data acquired in vivo without RF excitation. For Nyquist ghost correction,
190 three-line phase reference data (which characterize the gradient waveforms) were acquired in a
191 phantom immediately following each session, using the same multi-shot protocols as performed
192 in vivo. In pilot studies, this approach was observed to be more effective in reducing Nyquist
193 ghosting than using navigators from the in vivo data. The in vivo data did include a three-line
194 navigator for each shot, which was used for per-shot frequency offset demodulation. The
195 frequency offset per shot was estimated based on a magnitude-weighted coil combination of the
196 phase at the center of k-space in the second navigator echo, unwrapping the phase estimates
197 between shots. The frequency offset demodulation was necessary to reduce ghosting caused by
198 temporal B_0 field fluctuations (38).

	Single-Shot	4-Shot	4-Shot
In-Plane Resolution	**0.75 mm**	**0.75 mm**	**0.60 mm**
Slices and Thickness	24 at 3 mm	24 at 3 mm	24 at 3 mm
TR	1500 ms	746 ms	1100 ms
VAT	1500 ms	2984 ms	4400 ms
TE	20.8 ms	18 ms	26 ms
Nominal Flip Angle	68°	45°	56°
FOV Read	84 mm	128 mm	128 mm
Matrix	112	168	216
Bandwidth	1088 Hz/px	1144 Hz/px	890 Hz/px
Echo Spacing	1.04 ms	1.06 ms	1.31 ms
Effective PE Bandwidth	23 Hz/mm	59 Hz/mm	48 Hz/mm
Lines per Shot	41	21	27
Phase Partial Fourier	6/8	Off	Off
Acceleration	GRAPPA R = 2	SENSE R = 2	SENSE R = 2
Measurements	400	202	137
Saturation Slab	1 Anterior	None	None

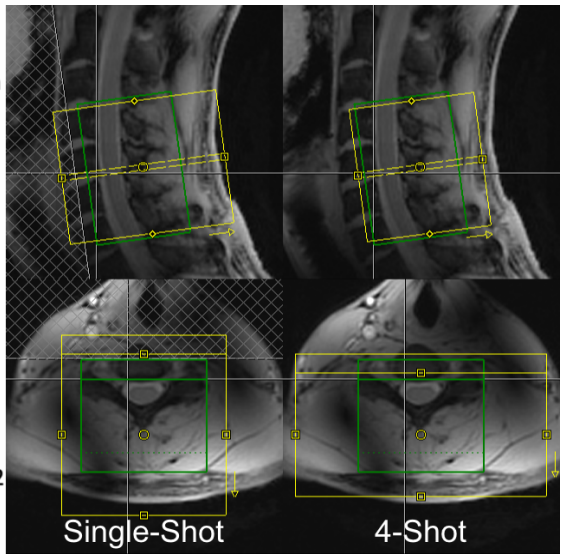

Figure 1: Pulse sequence parameters and slice positioning for three fMRI protocols.

To compare expected advantages and disadvantages between the protocols, Table 1 lists performance considerations relevant to BOLD fMRI, and for each of these gives the governing protocol parameters, and the expected relative ranking of the three candidate protocols. The relative importance of the different performance considerations, and the holistic ranking of protocol performance in cervical spinal cord BOLD fMRI at 7 T, is not obvious; the goal of this study is to determine this experimentally.

Performance Consideration	Governing Parameter(s)	Expected Ranking
BOLD Sensitivity	TE	**MS60** > SS75 > MS75
Signal Dropout	TE	**MS75** > SS75 > MS60
Ghosting	Number of Shots, TE	**SS75** > MS75 > MS60
Partial Fourier Blurring	Partial Fourier Factor	**MS60 ≈ MS75** > SS75
T2* Decay Blurring	Effective Phase Encode Bandwidth (dk/dt)	**MS75** > MS60 > SS75
Susceptibility-Induced Distortion	Effective Phase Encode Bandwidth (dk/dt)	**MS75** > MS60 > SS75

Table 1: Performance considerations relevant to BOLD fMRI, the protocol parameters governing performance regarding each image quality or sensitivity consideration, and the expected performance of the three candidate protocols relative to each other.

For each of the three imaging protocols, a 10-minute fMRI acquisition was performed with noxious thermal stimulation applied to the lateral surface of the base of the right thumb with a 30 mm x 30 mm flat thermode at a pre-calibrated intensity of 3/10 (range 42-51°C, average 46.5°C)

using an fMRI-compatible thermal stimulator (TSA-II, Medoc, Israel). Pain scale anchors were 0 = no pain and 10 = worst pain imaginable. Stimulus blocks were 10 seconds in duration, calculated by including ramp-up and plateau, but excluding ramp-down to baseline. Ramp speed was set to 10°C/sec. Stimulus blocks were separated by pseudo-randomized inter-stimulus intervals ranging from 25 to 45 seconds, plus initial and final stimulus-free blocks. This stimulus was expected to produce sensory activation in the ipsilateral dorsal horn at the neurological C6 (approximately vertebral C4-C5) level (45,46). Subjects were coached to remain still and maintain steady respiration during thermal stimuli. Pulse-oximeter and respiratory traces were acquired (TSD200, PPG100C, TSD201, and RSP100C, Biopac, Goleta, CA, USA).

Spinal cord toolbox v5.4.0 (47) was used for image pre-processing. Anatomical MP2RAGE images were segmented using *sct_deepseg_sc*, vertebral levels were labeled using *sct_label_vertebrae* and/or *sct_label_utils*. Registration to the PAM50 template (48) was performed using *sct_register_to_template*. Each 4-D fMRI dataset was motion-corrected using *sct_fmri_moco* with an inclusive cylindrical mask that contains the posterior neck muscle, the spinal canal and spinal cord were manually masked in FSLeyes (49), and the fMRI dataset was registered to the PAM50 template using *sct_register_multimodal*, initialized using the transformation calculated between the anatomical image and PAM50. Each fMRI dataset was straightened, spatially smoothed using *sct_smooth_spinalcord* with an anisotropic 2 mm x 2 mm x 6 mm Gaussian kernel oriented along the spinal cord centerline, and unstraightened, to minimize blurring of CSF signal into the cord.

First-level GLM analyses was performed in individual-subject space using FSL FEAT (50), incorporating autocorrelation correction and a 35-term physiological noise model (PNM) (31,51). The PNM was generated separately for each slice, incorporating slice timing correction, using FSL PNM, and included 8 cardiac phase, 8 respiratory phase, 16 cardiac-respiratory interaction, CSF signal derived from the spinal canal mask (canal mask minus cord mask), and two in-plane translational motion correction terms from *sct_fmri_moco*. Group-level GLM analysis was also performed in FSL FEAT using a mixed-effects model after warping the results of first-level analyses into PAM50 template space.

Temporal signal to noise ratio (tSNR) was calculated voxelwise as the ratio of temporal mean to standard deviation, then averaged within neurological level C6 in the PAM50 cord, gray matter, and white matter masks after motion correction, but before smoothing and application of the PNM. The extent of this neurological C6 mask was defined generously as the region where the probabilistic mask of C6 contained within SCT (52) is greater than zero. Several additional ROI

masks were defined for further analysis (Figure 2). The PAM50 cord mask, eroded by 1 voxel, was used to mask parameter maps for visualization. A mask for expected true-positive activation was constructed by summing the PAM50 masks for the right dorsal horn, right fasciculus gracilis, right fasciculus cuneatus, and right lateral corticospinal tract (PAM50 atlas mask entries 1, 3, 5, and 35), binarizing, eroding by one voxel from the cord-CSF border only, and calculating the intersection of the result with the aforementioned PAM50 mask for spinal (i.e., neurological) level C6 thresholded at zero. White matter structures were included to enclose potential BOLD signal in veins draining the expected gray matter site of activation (53), but the spinal venous plexus on the exterior of the spinal cord, though expected to also exhibit BOLD activation (54), was excluded due to the strong effects of CSF signal that cannot be fully accounted for by a PNM and the resulting strong potential for false-positive activation. A control mask, for comparison purposes, was calculated similarly using PAM50 masks for the left lateral corticospinal tract, left rubrospinal tract, left spinothalamic and spinoreticular tracts, and left ventral horn (PAM50 mask entries 4, 8, 12, and 30). These masks were also warped to each individual subject space. Although studies in rats have shown that some contralateral ventral horn activation does occur in response to noxious stimuli (55,56), this was judged to be the most suitable control region in light of the stronger resting-state connectivity between ipsilateral dorsal and ventral horns, and between ipsilateral and contralateral dorsal horns, in humans (12,13,57).

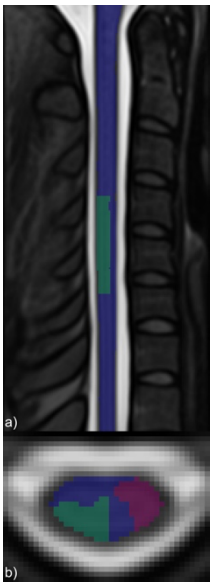

Figure 2: Masks used for analysis of task fMRI activation, displayed in PAM50 template space. The PAM50 cord mask, eroded by 1 voxel (blue), was used to mask parameter maps for visualization. Masks representing regions of interest in the C6 spinal level for expected true positive activation (green) and control (red)

are also displayed.

An uncorrected threshold of $z > 1.64$, which corresponds to a one-tailed p-value of 0.05, was chosen for thresholding of activation maps. For the group-level and each individual-subject result, the mean and maximum z-statistic across activated ($z > 1.64$) voxels within the true-positive and control ROI masks were tabulated. The ratio of the maximum z-statistic in the true-positive ROI mask to the maximum z-statistic in the control ROI mask in each subject was taken as a measure of the specificity of each protocol to true-positive activation. Mean BOLD percent signal change (PSC) was calculated in activated native space voxels in the true-positive region for each subject, and the BOLD percent signal change in the voxel in the true-positive region having the highest z-statistic in each subject was also tabulated.

Results

Individual subject-level mean and single-timeframe images and tSNR maps of datasets representing the best-case and worst-case image quality in the study are shown in Figure 3. These best-case and worst-case datasets were chosen by first selecting the subsets of cases with the highest and lowest tSNR, and from those subsets, choosing the dataset with the lowest and highest artifact burden by visual inspection, respectively. In axial slices near intervertebral junctions, where residual B_0 inhomogeneity is large, signal loss due to through-slice dephasing and geometric distortion are evident. Geometric distortion was less severe in multi-shot acquisitions, which had higher effective phase encoding bandwidth. The single-shot EPI had a blurrier appearance than the multi-shot acquisitions, while multi-shot 0.60 mm produced the sharpest appearing images. A spatial gradient in tSNR was also evident, with lower tSNR at more inferior levels. This resulted from a combination of reduced B_1^+ efficiency, increased static B_0 inhomogeneity, and larger time-varying B_0 fluctuations due to the proximity to the lungs.

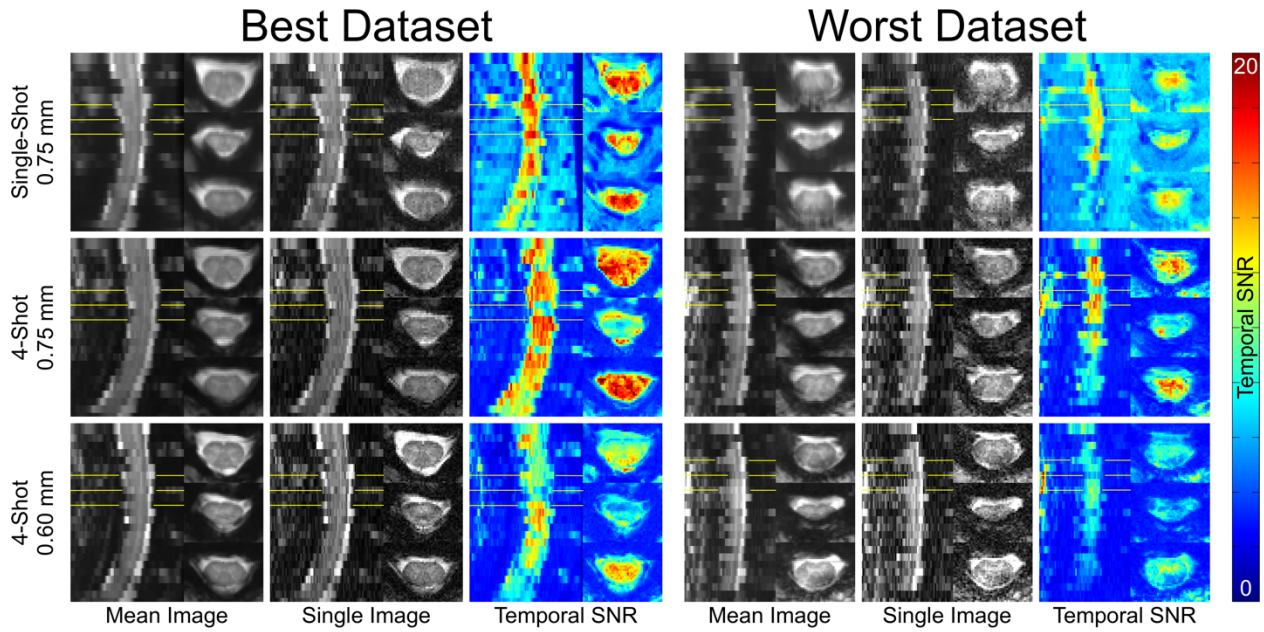

Figure 3: Individual subject-level images and temporal signal to noise ratio (tSNR) maps spanning C4-C7 vertebral levels in datasets representing best and worst image quality in the study. Locations of the three axial slices are indicated with yellow lines in the sagittal frames. The first and third displayed axial slices are superior and inferior to an intervertebral disc, and the second axial slice is located at an intervertebral disc.

Descriptive statistics of tSNR are given in Table 2. Temporal SNR was generally highest in single-shot 0.75 mm and multi-shot 0.75 mm, with lower variability between subjects in multi-shot 0.75 mm, while tSNR was significantly lower in multi-shot 0.6 mm, yet with lowest between-subject variability. Temporal SNR was slightly greater in gray matter than in white matter in all three protocols, driven predominantly by the higher signal in gray matter.

Temporal SNR in Neurological Level C6

	SS75	MS75	MS60
tSNR in Cord	14.6 ± 4.2	14.2 ± 3.3	10.0 ± 2.5
tSNR in GM	15.4 ± 4.2	15.1 ± 3.7	10.8 ± 2.6
tSNR in WM	14.2 ± 4.2	13.7 ± 3.0	9.7 ± 2.5

Table 2: Summary statistics of temporal signal to noise ratio (tSNR) measurements in data from three protocols. Tabulated means and standard deviations are calculated from individual subject-level means within PAM50 masks. NB: standard deviations across subjects of mean tSNR in the cord, GM, and WM do indeed all round to 4.2; differences appear at the third decimal place.

Maps of z-statistics and BOLD percent signal changes in group-level GLM analyses are shown in Figure 4. Z-statistic maps are thresholded at an uncorrected threshold of z = 1.64. Clusters of activation appear in all three protocols in the right (ipsilateral) dorsal quadrant at the expected C6 neurological level, which is centered approximately at the C4-C5 intervertebral disc (see Figure 2 for superior-inferior extent). All images are displayed in radiological orientation convention. The ipsilateral activation appears in the same cross-sectional location in single-shot 0.75 mm and multi-shot 0.6 mm; however, this cluster is weaker and located more peripherally in multi-shot 0.75 mm. In single-shot 0.75 mm, a cluster also appears in the contralateral (left) dorsal horn.

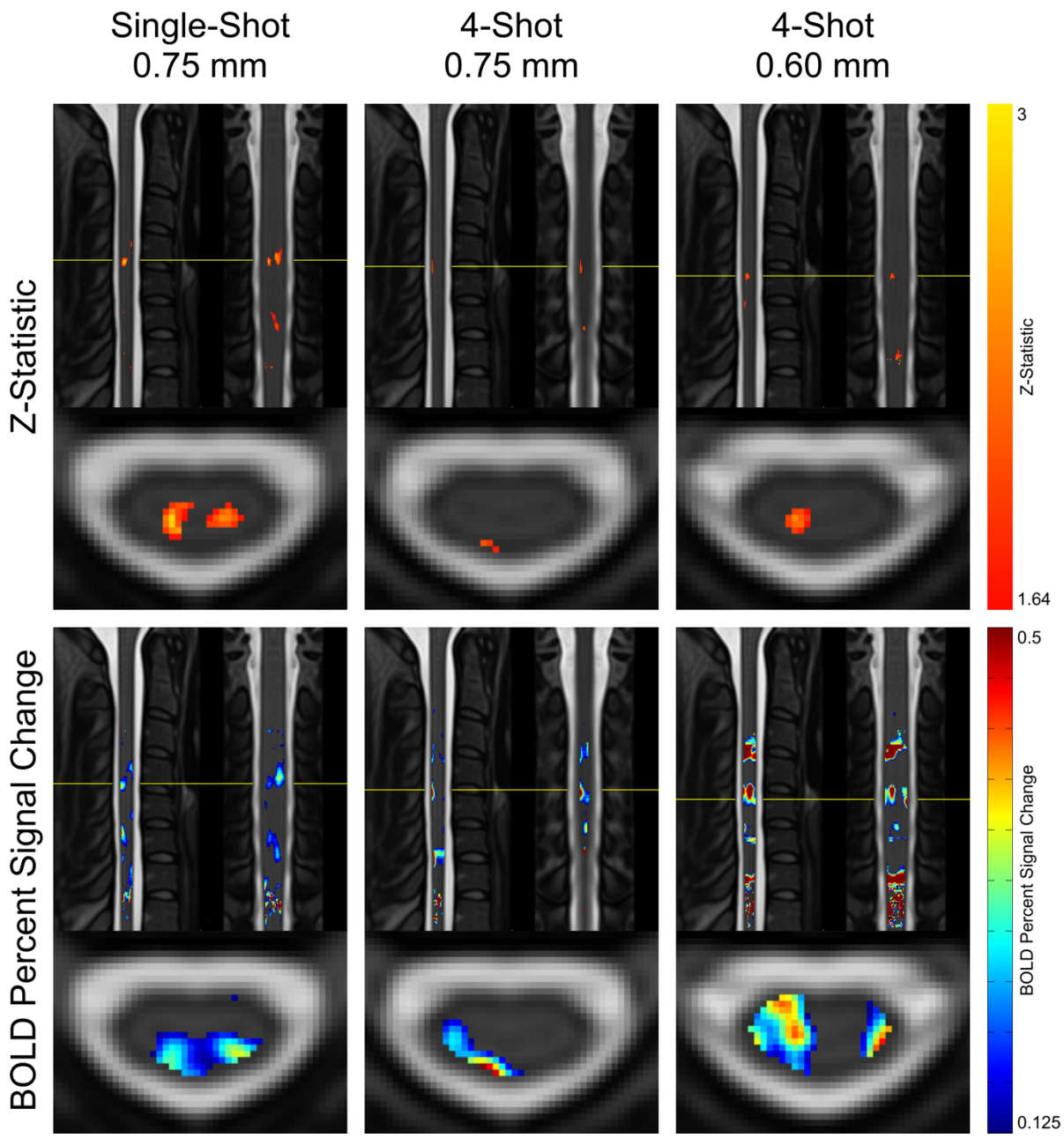

Figure 4: Maps of z-statistics and BOLD percent signal changes in group-level GLM analyses. Z-statistic maps are displayed using an uncorrected threshold of z = 1.64. Maps of BOLD percent signal change are thresholded for ease of visualization. Maps are masked to the spinal cord, encompassing all neurological levels, and the slice locations are centered on the voxel inside the spinal cord mask with the highest z-statistic.

Details of z-statistics and BOLD percent signal change in group-level GLM analyses are given in Table 3. Voxels within the true-positive and control ROI masks with z > 1.64 are considered activated. Mean z-statistics in activated true-positive voxels are relatively consistent in the range of 1.83 to 2.04 across the three protocols, with single-shot 0.75 mm yielding the highest mean z-statistic contrary to initial expectation (Table 1). The maximum true-positive z-statistic is highest in single-shot 0.75 mm at 2.85, compared to 2.07 in multi-shot 0.75 mm and 2.38 in multi-shot 0.6 mm. All three protocols yielded a ratio of true-positive to control max z-statistic between 1.27 and 1.37.

The mean BOLD percent signal change in activated voxels was higher in multi-shot datasets than in single-shot. Multi-shot 0.75 mm yielded the highest mean BOLD percent signal change, at 0.43%, and the BOLD percent signal change in the voxel with the highest z-statistic was 0.50%.

Group-Level Activation Results

Threshold for Significance is Z > 1.64	SS75	MS75	MS60
Mean Z-Stat in Activated Voxels in True Positive Region	2.04	1.83	1.84
Max Z-Stat in True Positive Region	2.85	2.07	2.38
Max Z-Stat in Control Region	2.24	1.51	1.83
Ratio of Max Z-Stat in True Positive vs. Control	1.27	1.37	1.30
Mean BOLD PSC in Activated Voxels	0.21	0.43	0.33
BOLD PSC in Voxel w/ Highest Z-Stat	0.22	0.50	0.38

Table 3: Summary statistics of group-level GLM results.

Maps of z-statistics and BOLD percent signal changes in two representative individual-level GLM analyses are shown in Figure 5 (best-quality dataset) and Figure 6 (worst-quality dataset). Z-statistic maps are thresholded at an uncorrected threshold of z = 1.64.

In the best-quality dataset in Figure 5, clusters of activation appear in the ipsilateral dorsal horn in all three protocols. The superior-inferior location of the peak activated cluster in the three protocols varies within this single subject to a greater extent than the expected size of a spinal segment in a single subject, although all three locations are contained within the group-level probabilistic PAM50 atlas entry for the C6 neurological level. In single-shot 0.75 mm, the cluster

extends into the ipsilateral ventral horn as well, and a smaller cluster appears in the contralateral deep dorsal horn. In multi-shot 0.75, a disconnected cluster of weak activation also appears in the ipsilateral ventral horn. The cluster in multi-shot 0.6 mm is intense and well-localized, coinciding with a cluster of high BOLD percent signal change approaching 2%. In the displayed slices, one likely false-positive voxel is visible at the contralateral cord-CSF boundary in the multi-shot 0.60 mm, and the contralateral cluster in single-shot 0.75 mm is neither clearly true-positive nor false-positive, but for the purpose of this analysis, a portion of it falls within the control mask ROI, and is treated as such in descriptive statistics.

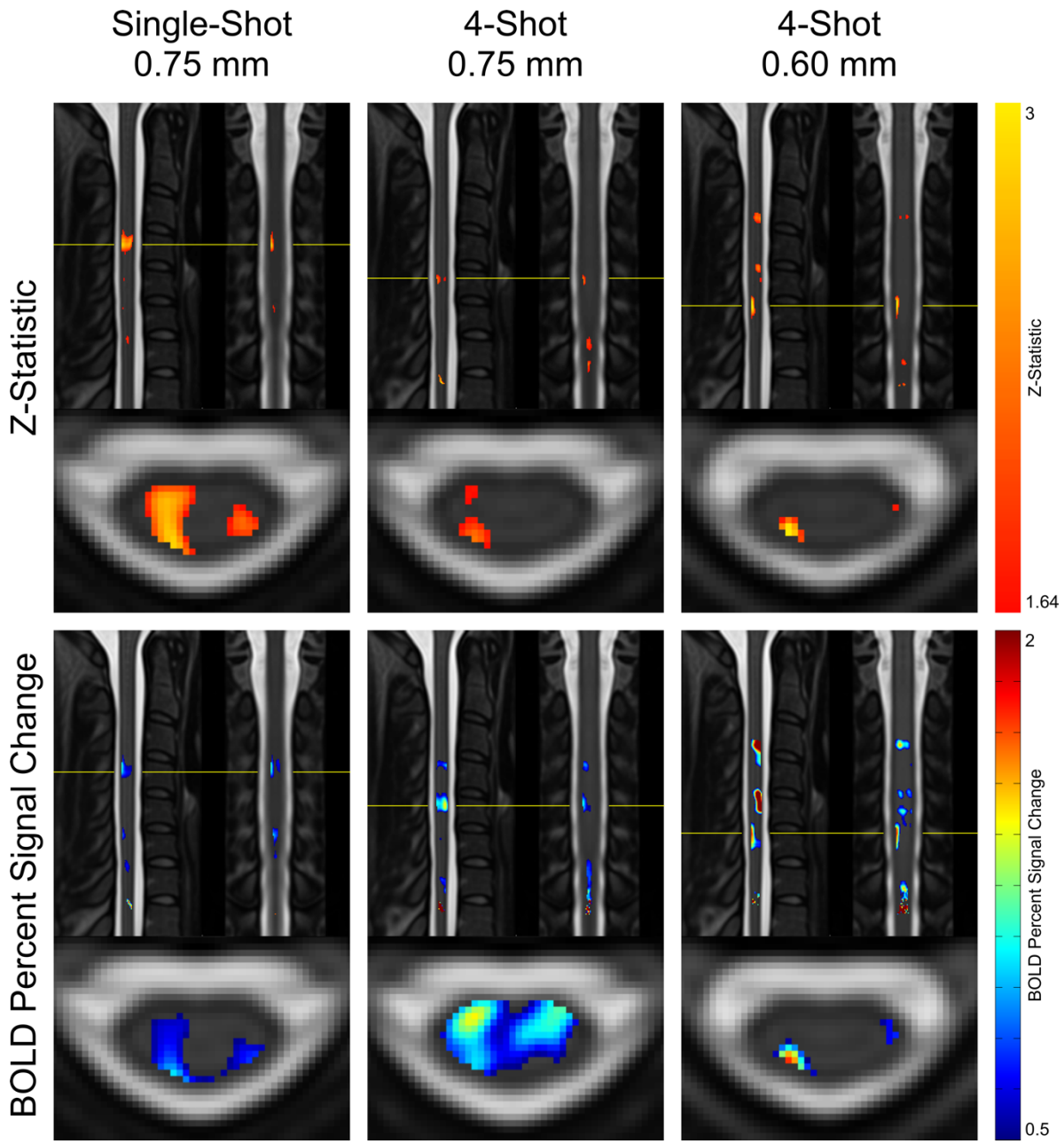

Figure 5: Individual subject-level maps of activation z-statistic and BOLD percent signal change, warped into template space, in the “best quality” dataset from Figure 2. Slice locations are centered on the voxel with the highest z-statistic.

In the worst-quality dataset in Figure 6, potentially plausible true-positive activation is visible in the ipsilateral dorsal quadrant in the multi-shot 0.6 mm protocol, though this cluster extends partially out of the superior boundary of the neurological C6 level. No activation exceeding the threshold of z = 1.64 is visible in either the single-shot or multi-shot 0.75 mm protocols. The location of the peak (although still sub-threshold) z-statistic within the true-positive mask ROI is indicated with a green crosshair in the axial plane, and yellow lines in the sagittal and coronal planes.

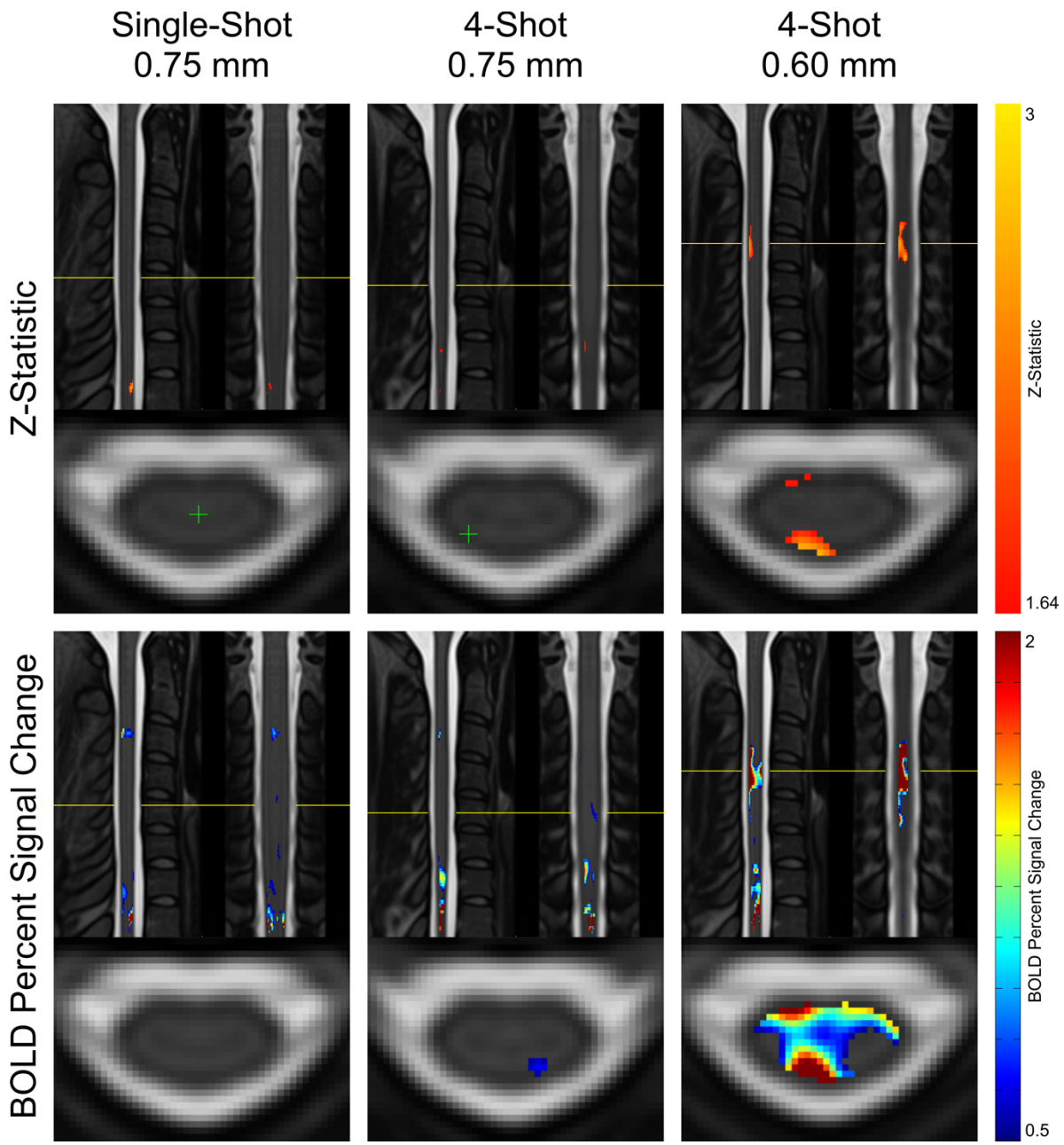

Figure 6: Individual subject-level activation maps, warped into template space, in the "worst quality" dataset from Figure 2. For single-shot 0.75 mm and 4-shot 0.75 mm, the images are centered at the voxel in the true positive region with the highest z-statistic (indicated with a green crosshair), but this z-statistic is below the threshold of 1.64.

Details of z-statistics and BOLD percent signal change across all individual-level GLM analyses are given in Table 4. As in group-level analyses, voxels within the true-positive and control ROI masks (warped to each individual subject space) with z > 1.64 are considered activated. Mean z-

statistics in activated true-positive voxels are relatively consistent in the range of 1.96 to 2.18 across the three protocols. Single-shot 0.75 mm yields the highest mean z-statistic, but the standard deviation of each subject's mean z-statistic in activated true-positive voxels is double that of the multi-shot protocols. Single-shot 0.75 mm also yields the highest mean maximum z-statistic at 2.68, compared to 2.27 for multi-shot 0.75 mm and 2.45 for multi-shot 0.6 mm. Single-shot 0.75 mm and multi-shot 0.6 mm have true-positive-to-control ratios substantially greater than unity, while the ratio in multi-shot 0.75 mm is closer to unity.

Similar to group-level analyses, the mean BOLD percent signal change in activated voxels was higher in multi-shot protocols. Multi-shot 0.6 mm yielded the highest mean BOLD percent signal change, at 1.78% ± 0.89%, followed by multi-shot 0.75 mm at 1.29% ± 0.76%, and single-shot 0.75 mm at 0.67% ± 0.31%. The same relationship among the protocols is evident in the BOLD percent signal change in the voxel with the highest z-statistic in each dataset.

Individual-Level Activation Results

Threshold for Significance in Z > 1.64	SS75	MS75	MS60
Mean Z-Stat in Activated Voxels in True Positive Region	2.18 ± 0.37	1.99 ± 0.17	1.96 ± 0.19
Max Z-Stat in True Positive Region	2.68 ± 1.41	2.27 ± 0.77	2.45 ± 0.55
Max Z-Stat in Control Region	2.27 ± 1.10	2.14 ± 0.76	2.11 ± 0.78
Ratio of Max Z-Stat in True Positive vs. Control	1.18	1.06	1.16
Mean BOLD PSC in Activated Voxels	0.67 ± 0.31	1.29 ± 0.76	1.78 ± 0.89
BOLD PSC in Voxel w/ Highest Z-Stat	0.88 ± 0.84	1.51 ± 1.07	2.11 ± 1.18

Table 4: Summary statistics of individual subject GLM analyses. In individual subjects, mean z-statistics and mean BOLD percent signal change (PSC) are calculated within voxels having z > 1.64, as well as BOLD PSC in the voxel having the highest z-statistic. Maximum z-statistics in true positive and control regions are calculated without a threshold on z-statistic. Means and standard deviations across these individual-subject mean and maximum values are then calculated and tabulated here.

Discussion

Image quality and tSNR are strongly impaired in spinal cord fMRI by static focal B_0 inhomogeneity near the intervertebral junctions and temporally variable B_0 inhomogeneity arising from the lungs. These two sources of B_0 inhomogeneity were clearly evident in the images and tSNR maps shown in Figure 3. Near the intervertebral junctions, tSNR was sharply reduced and geometric distortion and signal loss were markedly more severe than in slices further from a junction. The gradual reduction in tSNR in lower slices was partially due to static and dynamic B_0

inhomogeneity from the lungs, but reduced B_1^+ efficiency in the lower cervical spine was also a significant contributor (39); signal intensity in mean and single images was lower adjacent to vertebral level C7, compared to C4-C6, even in the best-quality dataset.

In general, the single-shot 0.75 mm protocol provided the greatest sensitivity (albeit highest between subject variability in z-statistics) to the expected activation, but also appeared to have the lowest effective in-plane resolution and largest geometric distortion. This was in line with expectations (Table 1), as the lower effective phase-encode bandwidth makes it more susceptible to T_2* blurring and geometric distortion due to static B_0 inhomogeneity, on top of blurring due to partial Fourier acquisition. Multi-shot 0.6 mm produced the most well-localized activation clusters, and the sharpest images, while being qualitatively less affected by geometric distortion caused by static B_0 inhomogeneity than single-shot 0.75 mm. However, sensitivity to activation was reduced due to its longer VAT, which reduced the number of time points in an experiment of fixed duration, and the lower tSNR, both of which reduce the statistical power. Multi-shot 0.75 mm generally performed poorly; it neither showed the sensitivity to activation of the single-shot 0.75 mm protocol nor the spatial specificity of the multi-shot 0.60 mm protocol, as if sharing the drawbacks of each of the other protocols, without enjoying the benefits of either protocol to a similar degree.

Decades of results in the brain have consistently shown that longer TEs (i.e., close to the T_2* of gray matter) are associated with greater sensitivity to activation. In the spinal cord at 7 T, however, the detrimental effects of B_0 inhomogeneity severely impair data quality at longer Tes. A balance must be struck between image quality, which favors shorter TE, and sensitivity to BOLD signal, which favors TE close to T_2* of gray matter, which is 29.3 ± 4.5 ms at 7 T (58). The optimal TE for a given spinal cord fMRI pulse sequence will therefore likely be shorter than the T_2* of gray matter.

In group-level GLM analyses, single-shot 0.75 mm and multi-shot 0.6 mm appeared to yield similarly-sized activation clusters, and the maximum z-statistic in single-shot 0.75 mm was substantially greater than the maximum z-statistic in multi-shot 0.6 mm (see Figure 4). In individual-level results, however, multi-shot 0.6 mm generally yielded more sharply-defined activation clusters in the ipsilateral dorsal quadrant (see Figure 5), and the difference between the maximum z-statistic in single-shot 0.75 mm and the maximum z-statistic in multi-shot 0.6 mm was much smaller than in the group level analysis. A possible explanation that unifies these observations is that multi-shot 0.6 mm was better able to spatially resolve activation in individual subjects, resulting in small clusters; however, when multiple subjects' data was combined, the inherent physiological variability in the location of activation among different subjects (52), as well

437 as potential limitations in group-level registration of distorted spinal cord EPI images, resulted in
438 these sharply-defined individual-level activation clusters spatially coinciding less fully in multi-shot
439 0.6 mm than did the broader activation clusters in single-shot 0.75 mm. These broader activation
440 clusters in single-shot EPI may have arisen due to its greater statistical power, having more
441 temporal frames due to a shorter volume acquisition time and higher tSNR due to the lower
442 effective resolution.

443 Based on TE, BOLD percent signal change would be expected to be highest in multi-shot 0.60
444 mm, followed by single-shot 0.75 mm and then multi-shot 0.75 mm. In individual-level results,
445 multi-shot 0.60 mm did indeed yield the highest BOLD percent signal change. However, of the
446 remaining two protocols, multi-shot 0.75 mm yielded higher BOLD percent signal change than
447 single-shot 0.75 mm. One potential explanation for this is that the effect of spatial resolution
448 outweighed the effect of the magnitude of the underlying BOLD activation in these individual-level
449 measurements; the multi-shot 0.75 mm acquisition is expected to better resolve BOLD activation
450 than the single-shot 0.75 mm acquisition. An alternative explanation specifically concerning the
451 difference in the mean BOLD percent signal change in activated voxels between the multi-shot
452 0.75 mm and single-shot 0.75 mm acquisitions is that the single-shot 0.75 mm acquisition, which
453 contained 400 temporal frames, was statistically better powered to detect low-BOLD-percent-
454 signal-change activation than the multi-shot 0.75 mm acquisition, which contained only 202
455 temporal frames and may have been additionally hampered by greater physiologic noise
456 contributions (e.g., ghosting). In other words, a voxel with a low BOLD percent signal change is
457 more likely to be identified as significantly activated using a protocol with a larger number of
458 temporal frames and less susceptibility to ghosting. This would result in a greater number of low-
459 BOLD-percent-signal-change voxels being included in the set of significantly activated voxels in
460 the single-shot 0.75 mm acquisition, depressing the mean BOLD percent signal change
461 calculated for that set of voxels.

462 The superior-inferior location of peak activation was similar across the three protocols in group-
463 level analyses, and appeared at the expected location in the center of neurological C6
464 (determined from the probabilistic spinal levels from the PAM50 atlas), based on the anatomical
465 location of the thermal stimulus. The superior-inferior location of the peak activation was expected
466 to vary across subjects due to natural physiological variation (52), but was not expected to vary
467 among the three protocols within each subject. Contrary to this expectation, we did observe
468 substantial variation in the superior-inferior location of peak activation of up to 1 ½ vertebral levels
469 across the three protocols within individual subjects (see Figure 5). The cause for this variation is

470 unclear without conducting a reproducibility study by repeating all three protocols on the same
471 participants. If the true underlying stimulus-related activation occurs across a large spatial extent
472 in the superior-inferior dimension, then random noise as well as variations in physiological noise
473 may shift the center of the detected activation between acquisitions in an unsystematic way, as
474 observed. In that case, increasing the sensitivity to detect BOLD responses, e.g. by acquiring for
475 longer, should yield extended activation clusters. The true underlying activation is however
476 unknown, and the data in this work cannot convincingly support any conclusion. From resting-
477 state studies, we would expect networks of correlated activity stretching over approximately one
478 vertebral level (57). Task-activated networks, and patterns of nociceptive activation in particular
479 may, however, have a broader spatial extent to resting-state networks due to the fact that primary
480 afferent projections may ascend or descend in Lissauer's tract before synapsing (59–61). A large
481 spatial extent of the activated networks in the superior-inferior dimension may even be a
482 prerequisite to detect activation clusters in group-level analyses with relatively few subjects. If the
483 activation were narrowly localized within one subject, with a variable center along the vertebral
484 levels between subjects, the statistical power to detect activation at the group level would be much
485 diluted. Further studies would be needed to investigate the true extent of the activation, and the
486 reproducibility of individual-level activation clusters.

487 Several groups have developed methods to address distortion and through-slice dephasing in
488 single-shot GRE EPI at 3 T through slicewise dynamic shimming methods using either slice-
489 specific gradient offsets (62) or z-gradient refocusing blips (63,64). These methods, applied to
490 single-shot EPI, may be promising alternatives to multi-shot 2D or 3D EPI at 7 T but, at the time
491 of this study, were not sufficiently refined to implement routinely at 7 T. Also 3D multi-shot EPI
492 sequences suitable for implementation in fMRI experiments were not readily available at the time
493 of this study, despite encouraging results demonstrating their robustness to B_0 inhomogeneity in
494 resting-state fMRI studies at 7 T (12,13). Such sequences remain a highly promising option worthy
495 of future investigation.

496 Conclusions

497 This study provides, to our knowledge, the first stimulus task fMRI results achieved in the spinal
498 cord at 7 T. For a given scan time, single-shot 0.75 mm was most sensitive to the expected
499 activation, likely due to its shorter volume acquisition time and greater statistical power, while
500 multi-shot 0.60 mm provided the best-localized activation clusters and the least geometric
501 distortion. The best choice of protocol will likely depend on the relative importance of sensitivity
502 to activation versus spatial localization of activation for a given experiment.

Acknowledgements

This study was supported by National Institutes of Health (NINDS) award K01NS105160 (ACS) and Department of Defense MSRP grant W81XWH-17-1-0204 (JX). The work was also supported by the Wellcome Trust (Strategic Award 102645/Z/13/Z, Senior Research Fellowship 202788/Z/16/Z). The Wellcome Centre for Integrative Neuroimaging is supported by core funding from the Wellcome Trust (203139/Z/16/Z). Data in this study was acquired using the University of Minnesota Center for Magnetic Resonance Research (CMRR) Multiband EPI pulse sequence software package. Portions of this study in smaller numbers of subjects have previously been presented as conference abstracts (53,65).

References

1. Minassian K, Hofstoetter US, Dzeladini F, Guertin PA, Ijspeert A. The Human Central Pattern Generator for Locomotion: Does It Exist and Contribute to Walking? Neuroscientist 2017;23:649–663 doi: 10.1177/1073858417699790.

2. Bingel U, Tracey I. Imaging CNS modulation of pain in humans. Physiology (Bethesda) 2008;23:371–380 doi: 10.1152/physiol.00024.2008.

3. Raj D, Anderson AW, Gore JC. Respiratory effects in human functional magnetic resonance imaging due to bulk susceptibility changes. Phys. Med. Biol. 2001;46:3331–3340 doi: 10.1088/0031-9155/46/12/318.

4. Vannesjo SJ, Miller KL, Clare S, Tracey I. Spatiotemporal characterization of breathing-induced B0 field fluctuations in the cervical spinal cord at 7T. NeuroImage 2017;167:191–202 doi: 10.1016/j.neuroimage.2017.11.031.

5. Krüger G, Glover GH. Physiological noise in oxygenation-sensitive magnetic resonance imaging: Physiological Noise in MRI. Magn. Reson. Med. 2001;46:631–637 doi: 10.1002/mrm.1240.

6. Cohen-Adad J. Functional Magnetic Resonance Imaging of the Spinal Cord: Current Status and Future Developments. Semin. Ultrasound CT MR 2017;38:176–186 doi: 10.1053/j.sult.2016.07.007.

7. Yacoub E, Shmuel A, Pfeuffer J, et al. Imaging brain function in humans at 7 Tesla. Magn. Reson. Med. 2001;45:588–594.

8. Gati JS, Menon RS, Ugurbil K, Rutt BK. Experimental determination of the BOLD field strength dependence in vessels and tissue. Magn. Reson. Med. 1997;38:296–302 doi: 10.1002/mrm.1910380220.

9. Triantafyllou C, Hoge RD, Krueger G, et al. Comparison of physiological noise at 1.5 T, 3 T and 7 T and optimization of fMRI acquisition parameters. NeuroImage 2005;26:243–250 doi: 10.1016/j.neuroimage.2005.01.007.

538 10. Stroman PW, Wheeler-Kingshott C, Bacon M, et al. The current state-of-the-art of spinal cord
539 imaging: methods. NeuroImage 2014;84:1070–1081 doi: 10.1016/j.neuroimage.2013.04.124.

540 11. Barry RL, Vannesjo SJ, By S, Gore JC, Smith SA. Spinal cord MRI at 7T. NeuroImage
541 2018;168:437–451 doi: 10.1016/j.neuroimage.2017.07.003.

542 12. Barry RL, Smith SA, Dula AN, Gore JC. Resting state functional connectivity in the human
543 spinal cord. Elife 2014;3:e02812 doi: 10.7554/eLife.02812.

544 13. Barry RL, Rogers BP, Conrad BN, Smith SA, Gore JC. Reproducibility of resting state spinal
545 cord networks in healthy volunteers at 7 Tesla. NeuroImage 2016;133:31–40 doi:
546 10.1016/j.neuroimage.2016.02.058.

547 14. Conrad BN, Barry RL, Rogers BP, et al. Multiple sclerosis lesions affect intrinsic functional
548 connectivity of the spinal cord. Brain 2018 doi: 10.1093/brain/awy083.

549 15. Weber KA, Chen Y, Wang X, Kahnt T, Parrish TB. Functional magnetic resonance imaging of
550 the cervical spinal cord during thermal stimulation across consecutive runs. NeuroImage
551 2016;143:267–279 doi: 10.1016/j.neuroimage.2016.09.015.

552 16. Brooks J, Tracey I. From nociception to pain perception: imaging the spinal and supraspinal
553 pathways. J. Anat. 2005;207:19–33 doi: 10.1111/j.1469-7580.2005.00428.x.

554 17. Eippert F, Finsterbusch J, Bingel U, Buchel C. Direct evidence for spinal cord involvement in
555 placebo analgesia. Science 2009 doi: 10.1126/science.1067176).

556 18. Geuter S, Büchel C. Facilitation of pain in the human spinal cord by nocebo treatment. J.
557 Neurosci. 2013;33:13784–13790 doi: 10.1523/JNEUROSCI.2191-13.2013.

558 19. Tinnermann A, Geuter S, Sprenger C, Finsterbusch J, Buchel C. Interactions between brain
559 and spinal cord mediate value effects in nocebo hyperalgesia. Science 2017;358:105–108 doi:
560 10.1126/science.aan1221.

561 20. Staud R, Boissoneault J, Lai S, et al. Spinal Cord Neural Activity of Fibromyalgia Patients and
562 Healthy Controls During Temporal Summation of Pain: An fMRI Study. Journal of
563 Neurophysiology 2021:jn.00276.2021 doi: 10.1152/jn.00276.2021.

564 21. Yoshizawa T, Nose T, Moore GJ, Sillerud LO. Functional magnetic resonance imaging of
565 motor activation in the human cervical spinal cord. NeuroImage 1996;4:174–182 doi:
566 10.1006/nimg.1996.0068.

567 22. Stroman PW, Nance PW, Ryner LN. BOLD MRI of the human cervical spinal cord at 3 tesla.
568 Magn Reson Med 1999;42:571–576 doi: 10.1002/(sici)1522-2594(199909)42:3<571::aid-
569 mrm20>3.0.co;2-n.

570 23. Backes WH, Mess WH, Wilmink JT. Functional MR Imaging of the Cervical Spinal Cord by
571 Use of Median Nerve Stimulation and Fist Clenching. 2001:6.

572 24. Stroman PW, Ryner LN. Functional MRI of motor and sensory activation in the human spinal
573 cord. Magnetic Resonance Imaging 2001;19:27–32 doi: 10.1016/S0730-725X(01)00226-0.

25. Stroman PW, Krause V, Malisza KL, Frankenstein UN, Tomanek B. Functional magnetic resonance imaging of the human cervical spinal cord with stimulation of different sensory dermatomes. Magnetic Resonance Imaging 2002;20:1–6 doi: 10.1016/S0730-725X(02)00468-X.

26. Stroman P. Mapping of Neuronal Function in the Healthy and Injured Human Spinal Cord with Spinal fMRI. NeuroImage 2002;17:1854–1860 doi: 10.1006/nimg.2002.1305.

27. Stroman PW, Krause V, Malisza KL, Frankenstein UN, Tomanek B. Extravascular proton-density changes as a non-BOLD component of contrast in fMRI of the human spinal cord. Magn. Reson. Med. 2002;48:122–127 doi: 10.1002/mrm.10178.

28. Lawrence JM, Stroman PW, Kollias SS. Functional magnetic resonance imaging of the human spinal cord during vibration stimulation of different dermatomes. Neuroradiology 2008;50:273–280 doi: 10.1007/s00234-007-0338-6.

29. Govers N, Béghin J, Van Goethem JWM, et al. Functional MRI of the cervical spinal cord on 1.5 T with fingertapping: to what extent is it feasible? Neuroradiology 2007;49:73–81 doi: 10.1007/s00234-006-0162-4.

30. Giulietti G, Giove F, Garreffa G, Colonnese C, Mangia S, Maraviglia B. Characterization of the functional response in the human spinal cord: Impulse-response function and linearity. NeuroImage 2008;42:626–634 doi: 10.1016/j.neuroimage.2008.05.006.

31. Brooks JCW, Beckmann CF, Miller KL, et al. Physiological noise modelling for spinal functional magnetic resonance imaging studies. NeuroImage 2008;39:680–692 doi: 10.1016/j.neuroimage.2007.09.018.

32. Piché M, Cohen-Adad J, Nejad MK, et al. Characterization of cardiac-related noise in fMRI of the cervical spinal cord. Magnetic Resonance Imaging 2009;27:300–310 doi: 10.1016/j.mri.2008.07.019.

33. Eippert F, Kong Y, Winkler AM, et al. Investigating resting-state functional connectivity in the cervical spinal cord at 3T. NeuroImage 2016;147:589–601 doi: 10.1016/j.neuroimage.2016.12.072.

34. Weber KA, Chen Y, Wang X, Kahnt T, Parrish TB. Lateralization of cervical spinal cord activity during an isometric upper extremity motor task with functional magnetic resonance imaging. NeuroImage 2016;125:233–243 doi: 10.1016/j.neuroimage.2015.10.014.

35. Weber KA, Chen Y, Paliwal M, et al. Assessing the Spatial Distribution of Cervical Spinal Cord Activity during Tactile Stimulation of the Upper Extremity in Humans with Functional Magnetic Resonance Imaging. NeuroImage 2020:116905 doi: 10.1016/j.neuroimage.2020.116905.

36. Barry RL, Conrad BN, Maki S, et al. Multi-shot acquisitions for stimulus-evoked spinal cord BOLD fMRI. Magn Reson Med 2020:mrm.28570 doi: 10.1002/mrm.28570.

37. Barry RL, Strother SC, Gatenby JC, Gore JC. Data-driven optimization and evaluation of 2D EPI and 3D PRESTO for BOLD fMRI at 7 Tesla: I. Focal coverage. NeuroImage 2011;55:1034–1043 doi: 10.1016/j.neuroimage.2010.12.086.

38. Vannesjo SJ, Clare S, Kasper L, Tracey I, Miller KL. A method for correcting breathing-induced

field fluctuations in T2*-weighted spinal cord imaging using a respiratory trace. Magn. Reson. Med. 2019 doi: 10.1002/mrm.27664.

39. Zhang B, Seifert AC, Kim J-W, Borrello J, Xu J. 7 Tesla 22-channel wrap-around coil array for cervical spinal cord and brainstem imaging. Magn. Reson. Med. 2017;78:1623–1634 doi: 10.1002/mrm.26538.

40. Marques JP, Kober T, Krueger G, van der Zwaag W, Van de Moortele P-F, Gruetter R. MP2RAGE, a self bias-field corrected sequence for improved segmentation and T1-mapping at high field. NeuroImage 2010;49:1271–1281 doi: 10.1016/j.neuroimage.2009.10.002.

41. Griswold MA, Jakob PM, Heidemann RM, et al. Generalized autocalibrating partially parallel acquisitions (GRAPPA). Magn. Reson. Med. 2002;47:1202–1210 doi: 10.1002/mrm.10171.

42. Talagala SL, Sarlls JE, Liu S, Inati SJ. Improvement of temporal signal-to-noise ratio of GRAPPA accelerated echo planar imaging using a FLASH based calibration scan. Magn. Reson. Med. 2016;75:2362–2371 doi: 10.1002/mrm.25846.

43. Seifert AC, Xu J. Impact of autocalibration method on accelerated EPI of the cervical spinal cord at 7 T. Magnetic Resonance in Med 2022;88:2583–2591 doi: 10.1002/mrm.29415.

44. Pruessmann KP, Weiger M, Börnert P, Boesiger P. Advances in sensitivity encoding with arbitrary k-space trajectories: SENSE With Arbitrary k-Space Trajectories. Magn. Reson. Med. 2001;46:638–651 doi: 10.1002/mrm.1241.

45. Keegan JJ, Garrett FD. The segmental distribution of the cutaneous nerves in the limbs of man. Anat. Rec. 1948;102:409–437 doi: 10.1002/ar.1091020403.

46. Lee MWL, McPhee RW, Stringer MD. An evidence-based approach to human dermatomes. Clin. Anat. 2008;21:363–373 doi: 10.1002/ca.20636.

47. De Leener B, Lévy S, Dupont SM, et al. SCT: Spinal Cord Toolbox, an open-source software for processing spinal cord MRI data. NeuroImage 2017;145:24–43 doi: 10.1016/j.neuroimage.2016.10.009.

48. De Leener B, Fonov VS, Collins DL, Callot V, Stikov N, Cohen-Adad J. PAM50: Unbiased multimodal template of the brainstem and spinal cord aligned with the ICBM152 space. NeuroImage 2017;165:170–179 doi: 10.1016/j.neuroimage.2017.10.041.

49. Jenkinson M, Beckmann CF, Behrens TEJ, Woolrich MW, Smith SM. FSL. Neuroimage 2012;62:782–790 doi: 10.1016/j.neuroimage.2011.09.015.

50. Woolrich MW, Ripley BD, Brady M, Smith SM. Temporal autocorrelation in univariate linear modeling of FMRI data. Neuroimage 2001;14:1370–1386 doi: 10.1006/nimg.2001.0931.

51. Kong Y, Jenkinson M, Andersson J, Tracey I, Brooks JCW. Assessment of physiological noise modelling methods for functional imaging of the spinal cord. NeuroImage 2012;60:1538–1549 doi: 10.1016/j.neuroimage.2011.11.077.

52. Cadotte DW, Cadotte A, Cohen-Adad J, et al. Characterizing the location of spinal and vertebral levels in the human cervical spinal cord. AJNR Am J Neuroradiol 2015;36:803–810 doi:

10.3174/ajnr.A4192.

53. Seifert AC, Vannesjo SJ. Spatial Specificity of BOLD Signal in the Spinal Cord at 7T Using a Noxious Thermal Stimulus. Proceedings of the International Society for Magnetic Resonance in Medicine 2020:1168.

54. Cohen-Adad J, Gauthier CJ, Brooks JCW, et al. BOLD signal responses to controlled hypercapnia in human spinal cord. NeuroImage 2010;50:1074–1084 doi: 10.1016/j.neuroimage.2009.12.122.

55. Coghill RC, Price DD, Hayes RL, Mayer DJ. Spatial distribution of nociceptive processing in the rat spinal cord. Journal of Neurophysiology 1991;65:133–140 doi: 10.1152/jn.1991.65.1.133.

56. Coghill RC, Mayer DJ, Price DD. The roles of spatial recruitment and discharge frequency in spinal cord coding of pain: a combined electrophysiological and imaging investigation. Pain 1993;53:295–309 doi: 10.1016/0304-3959(93)90226-F.

57. Kong Y, Eippert F, Beckmann CF, et al. Intrinsically organized resting state networks in the human spinal cord. Proc. Natl. Acad. Sci. U.S.A. 2014;111:18067–18072 doi: 10.1073/pnas.1414293111.

58. Massire A, Taso M, Besson P, Guye M, Ranjeva J-P, Callot V. High-resolution multi-parametric quantitative magnetic resonance imaging of the human cervical spinal cord at 7T. NeuroImage 2016;143:58–69 doi: 10.1016/j.neuroimage.2016.08.055.

59. Coggeshall RE, Chung K, Chung JM, Langford LA. Primary afferent axons in the tract of lissauer in the monkey. J. Comp. Neurol. 1981;196:431–442 doi: 10.1002/cne.901960307.

60. Light AR, Perl ER. Spinal termination of functionally identified primary afferent neurons with slowly conducting myelinated fibers. J. Comp. Neurol. 1979;186:133–150 doi: 10.1002/cne.901860203.

61. Sugiura Y, Lee CL, Perl ER. Central Projections of Identified, Unmyelinated (C) Afferent Fibers Innervating Mammalian Skin. Science 1986;234:358–361 doi: 10.1126/science.3764416.

62. Islam H, Law CSW, Weber KA, Mackey SC, Glover GH. Dynamic per slice Shimming for Simultaneous Brain and Spinal Cord fMRI. Magn. Reson. Med. 2018 doi: 10.1002/mrm.27388.

63. Finsterbusch J, Eippert F, Büchel C. Single, slice-specific z-shim gradient pulses improve T2*-weighted imaging of the spinal cord. NeuroImage 2012;59:2307–2315 doi: 10.1016/j.neuroimage.2011.09.038.

64. Kaptan M, Vannesjo SJ, Mildner T, et al. Automated slice-specific z-shimming for functional magnetic resonance imaging of the human spinal cord. Human Brain Mapping 2022:hbm.26018 doi: 10.1002/hbm.26018.

65. Seifert AC, Vannesjo SJ. Comparison of Physiological Noise Models for Thermal Stimulus fMRI in the Cervical Spinal Cord at 7T. Proceedings of the International Society for Magnetic Resonance in Medicine 2022:1462.